



LAWRENCE  
LIVERMORE  
NATIONAL  
LABORATORY

# Validation of HADES-based Simulations of Radiographic Experiments at LLNL

H. Chen, M. Aufderheide, W. T. White, G. P.  
Roberson, L. Glascoe

June 23, 2011

IEEE International Conference on Technologies for Homeland  
Security

Waltham, MA, United States

November 15, 2011 through November 17, 2011

## **Disclaimer**

---

This document was prepared as an account of work sponsored by an agency of the United States government. Neither the United States government nor Lawrence Livermore National Security, LLC, nor any of their employees makes any warranty, expressed or implied, or assumes any legal liability or responsibility for the accuracy, completeness, or usefulness of any information, apparatus, product, or process disclosed, or represents that its use would not infringe privately owned rights. Reference herein to any specific commercial product, process, or service by trade name, trademark, manufacturer, or otherwise does not necessarily constitute or imply its endorsement, recommendation, or favoring by the United States government or Lawrence Livermore National Security, LLC. The views and opinions of authors expressed herein do not necessarily state or reflect those of the United States government or Lawrence Livermore National Security, LLC, and shall not be used for advertising or product endorsement purposes.

# Validation of HADES-based Simulations of Radiographic Experiments at LLNL

Haiyin Chen, Maurice B. Aufderheide III, *Member, IEEE*, W. Travis White III, G. Patrick Roberson  
and Lee G. Glascoe

Lawrence Livermore National Laboratory, Livermore, CA 94551 USA

**Abstract**—We have compared radiographic simulations generated with the HADES code against experimental radiographic measurements of a set of common materials of known composition and density: graphite, Teflon, Delrin, magnesium, silicon, titanium, and water cylinders. HADES calculations show good agreement with radiograph measurements. We analyzed discrepancy between simulation and experimental data and suggest sources of error and future improvement for the model.

**Keywords**—X-ray applications; Nondestructive testing; X-ray detection; X-ray modeling; Radiography simulation

## I. INTRODUCTION

There has been a great deal of effort recently to use X-ray detection systems to search for various kinds of contraband in luggage and cargo. Generally such systems attempt to identify offending materials through the use of polychromatic X-ray spectral sources (with endpoint energies less than roughly 300 keV and with varying amounts of filtration). By comparing images with different spectra, it is possible in principle to discriminate various materials.

Such an effort is challenging because X-rays at this energy have properties which complicate detection and interpretation. First, in this energy range, the attenuation of X-rays is strongly energy-dependent, making transmission measurements very sensitive to details of the X-ray spectrum. In addition, the measurements of such detection systems are a product of the source spectrum and the detector sensitivity and it is difficult to disentangle these properties of the system. In addition, scatter, both Compton and coherent, occurs in the imaged materials, and confuses the primary signal of attenuation through the cargo (particularly imaging systems with a wide field of view).

For a single experimental system, these issues could perhaps be resolved through careful instrument design and an extensive experimental program to calibrate the system using known materials. However, such an experimental program is expensive and may be impracticable when many different systems are in play. In addition, many of the types of contraband of interest can be extremely dangerous to fabricate and handle, adding to the cost of a purely empirical program.

Because of these challenges, we have been using radiographic simulation to assist in understanding X-ray absorption measurements in materials. Having a robust and accurate simulation tool may enable us to replace or

supplement experimentation on certain sensitive materials. An important early step in this work is validating the radiographic simulations with measurements from an actual radiographic system. This validation is the subject of this paper. In this paper, we describe the properties of the radiographic system, and how we perform the simulations. We then compare the simulations with experiment and discuss the implications of these results and future work.

## II. EXPERIMENTAL SETUP

### A. MicroCT System

For these studies we use a microCT system that produces large format pictures for use in reconstructing tomographic images of the samples of interest. For this paper, we only use a single radiographic image of the sample.

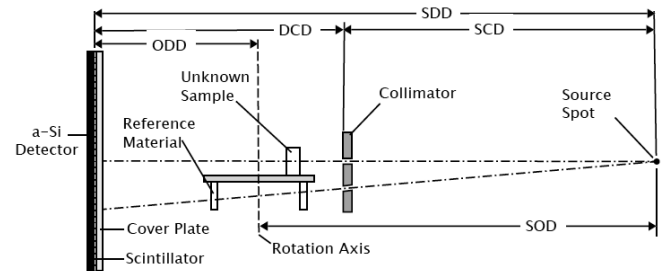


Fig. 1. Layout for microCT experiments and simulations. Here SDD is 140.25 cm, ODD is 29.55 cm, SOD is 110.66 cm, DCD is 44.57 cm and SCD is 95.68 cm. The rotation axis of the carousel is 3.4925 cm from the center of the main sample (called the “unknown” sample in the drawing). For the studies in this paper, the sample is in the position depicted.

The LLNL microCT system is depicted in Figure 1. Two thin X-ray fan beams pass through the sample area and are intercepted by a gadolinium oxysulfide (GOS) scintillator mounted to a Thales amorphous-silicon (aSi) area detector. The images on the detector are interpolated (3:2) from the 0.127-mm native pixel size to a 0.191-mm pixelated image. The two x-ray fans thus produce about 14-rows of data for each slit; the central rows are reconstructed using classical filtered back-projection techniques.

As shown in Figure 1, the sample is mounted on top of the sample plate (referred to as the “carousel”). Located around the perimeter of the lower level of the carousel are a set of (nominally) 1/2-inch diameter reference samples comprising graphite, ethanol, acetyl copolymer, water, Teflon, and a 6061-T6 aluminum alloy. The acetyl copolymer is typically referred

to as Delrin, which has a similar composition. The liquids are in polypropylene bottles. The reference samples, which are imaged simultaneously with the specimen, provide an image-quality reference that monitors scan-to-scan consistency.

### B. Samples and Data collection

The sample information is listed in Table 1. Several of the samples were purchased with specified purities from chemical supply distributors. Impurities, or uncertain composition, can affect the X-ray absorption and introduce errors in the model. The linear attenuation coefficient is proportional to material density. Where measured, the densities should be accurate to better than 2%.

Impurities in chemical content have a more complex effect on the measured attenuation. The 6061 aluminum alloy can be expected to have 1–2% content from the third row of the periodic chart (elements 20–30) and should show significantly more absorption than aluminum, particularly for the softest (100-kV) spectrum. The “Delrin” samples are actually an acetyl copolymer, which includes an unknown amount of ethylene oxide. Because the unknown content is relatively low-Z, this does not have as strong an effect as the impurities in the aluminum alloy.

To linearize the detector, we first captured images at three different X-ray beam intensities at a given voltage and filter setting on the source. The images are a dark field, bright field, and mid-range field. We then follow the manufacturer’s instructions pixel by pixel, normalizing the data to remove effects of detector saturation and spatial nonuniformity. The result is that an X-ray beam from a point source produces nominally the same count in every pixel (a “flat field”), despite detector non-uniformities and  $1/r^2$  fall-off of intensity across the detector panel.

Data were collected as full sets of computed-tomographic radiographs, with 400 radiographs (or views) taken at discrete steps over a 199.5-degree rotation of the carousel. Each view was averaged from four radiographic images (or frames). The spectral conditioning is described in Section IIIA. The HADES processing utilized only the single view where the specimen was closest to the source. For every data set (unique combination of sample and X-ray spectrum), a background image is collected without the sample in place.

## III. SIMULATION TECHNIQUE

In this study we use the HADES radiographic simulation code, which was developed for modeling radiographic image formation in a variety of nondestructive evaluation applications [1], [2]. HADES is a ray-tracing code that simulates X-ray radiography using as much fidelity to the physics of radiography as possible. For a user-specified source point, characterized as a binned X-ray spectrum, HADES casts a bundle of rays to the center of each pixel of a user-specified detector array. For each ray, HADES computes the attenuation along the path between the source point and detector pixel center. This attenuation is computed for each energy bin of the user-defined spectrum. HADES builds a stack of images, one for each bin of the source spectrum. After every ray has been computed, HADES blurs each image using an energy-

Sample Name	Diameter (cm)	Density (g/cm <sup>3</sup> )	Composition
Graphite 0.5’’	1.30	1.82	99.997%
Graphite 1’’	2.50	1.66	99.997%
Graphite 2’’	5.02	1.74	99.95%
Delrin 0.5’’	1.27	1.41*	nominal
Delrin 1’’	2.55	1.41	nominal
Delrin 2’’	5.09	1.40	nominal
Teflon 0.5’’	1.26	2.16*	nominal
Teflon 1’’	2.57	2.15	nominal
Teflon 2’’	5.53	2.17	nominal
Magnesium 0.5’’	1.29	1.74	99.9%
Magnesium 1’’	2.55	1.73	99.9%
Aluminum 1’’	2.56	2.70	6061 alloy
Silicon 0.5’’	1.26	2.32	99.999%
Silicon 1’’	2.53	2.32	99.999%
Titanium 0.5’’	1.29	4.49	99.99%
Water 0.5’’	1.08	1.00*	distilled, deionized
Water 1’’	2.72	1.00*	distilled, deionized
Water2’’	4.77	1.00*	distilled, deionized

Table 1. Physical Parameters of the Specimens. \* Nominal material densities were used in lieu of measurements.

dependent detector-blur function described below. The images are then summed using the product of the user-defined incident spectral distribution and the energy deposition computed using MCNP (described in Section IIIC) in the active region of the detector. One factor which enhances the fidelity of HADES simulations is the use of Monte Carlo codes such as MCNP [3] to build the source and detector models. The simulations developed for this study have three main components: a source model, collimation/object model, and detector model. These will be described in more detail below.

### A. Source Model

The YXLON Y.TU 450-D09 X-ray tube was modeled using the MCNP5 Monte Carlo code, using full electron-photon transport. The tungsten target is modeled as an oversized 1cm thick cylinder with radius of 150 cm. The incident electron beam impinges upon the center of this cylinder  $11^\circ$  from the cylinder normal (this angle corresponds to the  $11^\circ$  takeoff angle of the source). A beryllium window 5 mm thick is placed 5 cm from the point where the electrons hit the target, parallel to the incident angle of the electron beam. The spectrum of the resulting X-rays is tallied 20 cm from the impact point of the electrons,  $11^\circ$  above the top plane of the target cylinder. It has been found that the inclusion of the beryllium window does not have any effect on the source generation, except to attenuate the spectra.

In three separate simulations, electrons are sent into the target with energies of 100 keV, 160 keV and 300 keV and the resulting X-ray spectrum is collected in 71, 86 and 106 energy bins, respectively, up to the end-point energy. The 100 keV X-ray spectrum is then attenuated by a 1.943 mm aluminum filter. The 160 keV X-ray spectrum is then attenuated by either a 1.943 mm aluminum filter or 1.943 mm aluminum and 1.905 mm copper filters. The 300 keV X-ray spectrum is then attenuated by a 2.972 mm copper filter. These filtered spectra are depicted in Fig. 2.

In this discussion, we have neglected the issue of source size, which can be a contributor to blur at the imaging plane. However, for this system, the magnification of the sample

cylinder is 1.31, which means that the contribution of source blur is  $(0.31)^2 = 0.09$  of the contribution from blur at the detector, using a simple Gaussian approximation for both blurs. Hence, the contribution of source size is small compared to the detector contribution, and thus we neglect it in our study. HADES could include the effect if it were important.

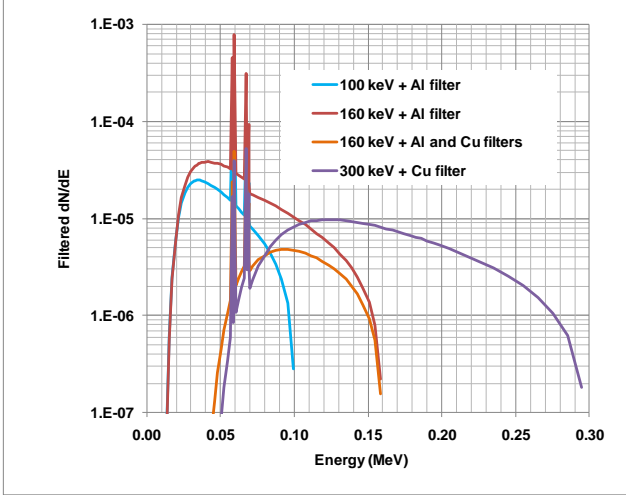


Fig. 2. Filtered spectra from YXLON source, as modeled for this study.

The attenuation of these filters as a function of energy was computed using the LLNL Evaluated Photon Data Library [4]. These spectra show the K-shell emission lines characteristic of tungsten and the underlying bremsstrahlung continuum. The overall effect of the filtration is to reduce the low-energy parts of each spectrum. This is particularly evident in the spectra which were filtered by copper. These filtered spectra are used as the inputs to the HADES simulations described below.

### B. Collimation/Object Model

The HADES code is linked to BRL-CAD, the US Army's open source CAD modeling library [5]. Because of this linking, it is possible to build CAD descriptions of objects using the BRL-CAD geometry editors and use HADES to simulate radiographs of the objects. We have made extensive use of this capability in this study.

In this CAD model, we have included the tungsten slit collimator, the sample being studied, as well as the carousel trays it is mounted on and reference samples included in each radiograph. It is possible to model the rotation of the samples on the carousel and simulate the data collection for tomographic reconstruction, but here we focus on the radiographs produced when the main sample is closest to the source. For each sample we have used measured density and size of the sample and the nominal composition. HADES uses the LLNL Evaluated Photon Data Library cross sections [5] to compute all attenuations, for which the photoelectric cross sections are an improvement over Hubbell's 1981 tables [6]. The other cross sections in [5] are taken from [6]. Cullen *et. al* quote an uncertainty of 3% for their photoelectric cross sections, while Hubbell quotes an uncertainty of "a few percent" for individual processes, such as incoherent scatter (Compton). Since these are the two dominant absorption

processes relevant here, it is prudent to assign roughly 5% uncertainty to the overall cross sections used in HADES in this energy range.

### C. Detector Model

How a detector converts X-ray signal into a measureable signal is an extremely complex process, generally not amenable to analytic treatments. In order to produce high fidelity simulations with HADES, we build an MCNP model of the X-ray and electron-photon transport within the detector and calculate the energy deposition in the scintillator, as representative of the detector response.

The THALES FlashScan 33 imaging detector is an amorphous silicon detector, which uses a Kodak Lanex fine scintillator to convert the X-ray and electron energy into light. The scintillation light is detected by photodiodes in the silicon panel. Direct electron and X-ray energy deposition in the photodiodes is not calculated. We have performed detailed MCNP models of a similar system in the past [7] and used this model for the simulations reported here.

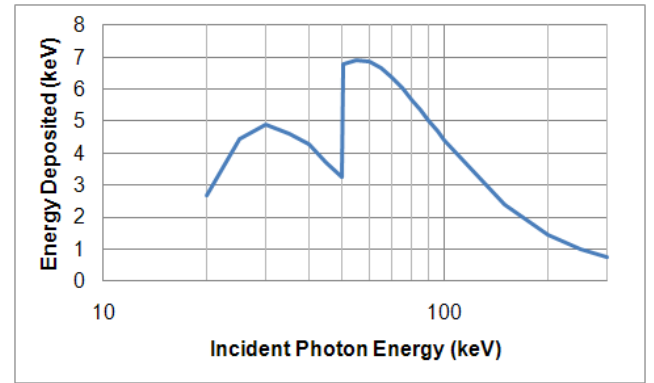


Fig. 3. Energy deposited in the detector as a function of the incident photon energy. The sudden rise in energy deposit at 50 keV is due to the gadolinium K-shell absorption edge in the Lanex scintillator.

This model is generated by performing many MCNP simulations, which model the energy deposited in the scintillator layer spatially as a function of incident X-ray energy. These responses are compiled and put into a library used by HADES. This library tells HADES how to weigh the image corresponding to each X-ray energy bin and also how to blur each image, since these properties depend on the energy of the X-rays impinging the detector. The relative weighting of the images by energy is given by the energy deposition curve, produced by the MCNP calculations. Fig. 3 shows this curve.

An important aspect of this modeling is that it indicates that amorphous silicon detectors have fairly high spatial resolution, but also have a large tail in their blur functions. This large tail comes from the production and transport of secondary electrons within the silicon and its glass substrate. These electrons sometimes are able to deposit energy into the scintillator. As a result, there are significant contributions of signals from up to 2 cm away being mixed into the local signal. In Fig. 4, we show the point spread function for various energies as calculated by MCNP.

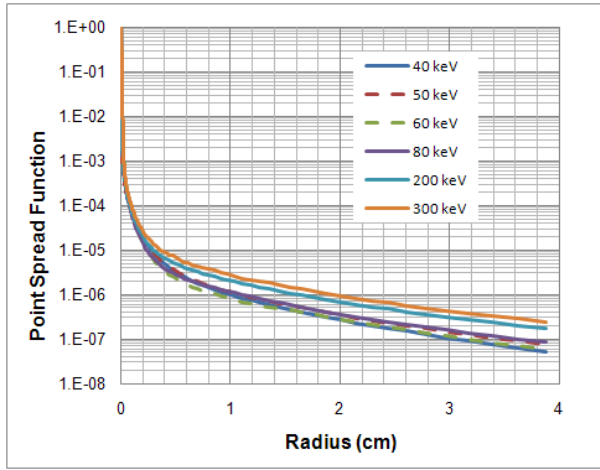


Fig. 4. Variation of detector point spread function with X-ray energy. It can be seen that, as incident photon energy increases, the tail of the PSF increases. All PSFs have been normalized by their respective 0 Radius values.

For most measurements, this system is highly collimated, which drastically reduces the contamination from X-ray scatter in the system. However, the rapid change in contrast at each of these slits results in a good deal of blurring from the large tails in the detector. As a result, the bright regions of the slit, which are fully transmitting, are blurred and somewhat darkened. For the 100 keV spectrum with aluminum filtration, the slit shows a maximum transmission of 90.5%. For the 160 keV spectrum with aluminum filtration, the slit shows a maximum transmission of 89.6%. For the 160 keV spectrum with aluminum and copper filtration, the slit shows a maximum transmission of 87.6%. For the 300 keV spectrum with copper filtration, the slit shows a maximum transmission of 85.6%. The amount of transmission decreases with increasing filtration because the effective energy of the spectrum is increasing, which leads to electrons with greater range affecting the detector, resulting in more blur.

This darkening indicates that the part of the image with the slits which are heavily mixed with information from the surrounding pixels. When making comparisons with the experimental images, it is necessary to recognize that the “full” transmission in the experimental images of the slit is not actually full transmission because of detector blur.

The HADES simulations are performed with the geometry defined above and the spectrum and detector characteristics summarized earlier. The images are defined to have a 60.96 cm X 42.662 cm field of view, so that blur effects are not affected by the edge of the detector. Pixel size is chosen to be 0.38 mm, which is twice the pixel size of the radiograph. The resulting simulated images are analyzed in a manner similar to the corrected experimental images.

#### IV. COMPARISON BETWEEN DATA AND SIMULATIONS

Figure 5 shows a pseudocolored radiographic image collected by the microCT on 1/2-inch thick magnesium cylinder, where the bright region across the middle of the image corresponds to the top slit of the collimator, and darkened area within the bright region corresponds to the sample. The blue trace to the left of the image provides the

average intensity across each rows of pixels of the slit. Only data from these 10 rows are used for subsequent image processing. row in the image. The flat region in the middle of the trace corresponds to the middle 10

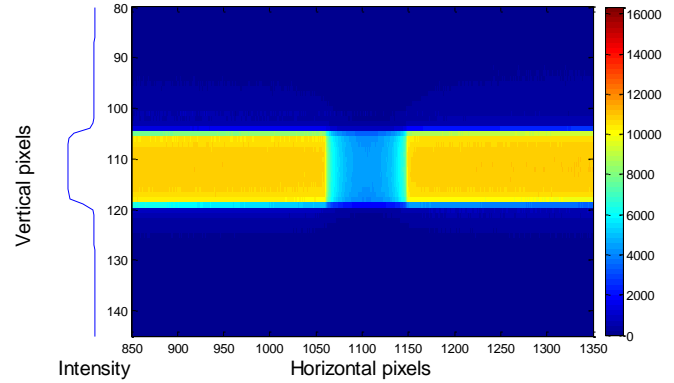


Fig. 5. Representative microCT radiographic image taken on half-inch diameter magnesium cylinder. Blue trace to the left of the image shows the average intensity across each row of pixels. Colorbar on right provides scale for pixel intensity.

Figure 6 provides an example of transmittance comparison between microCT measurements and HADES simulation. Transmittance,  $I/I_0$ , is computed by normalizing each radiograph image ( $I$ ) pixel-wise by a background image ( $I_0$ ) taken under the exact same experimental condition without any object between the collimator and the detector. Traces in Fig. 6 are derived from row 112 of the radiograph image shown in Fig. 5 and the corresponding data from HADES simulation.

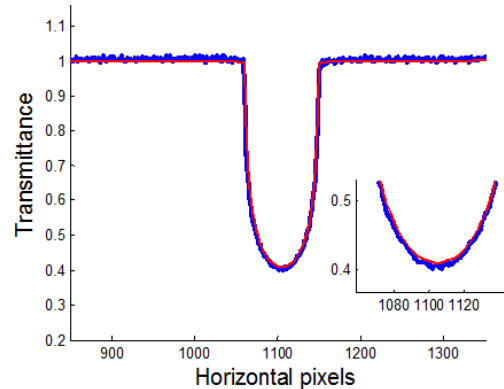


Fig. 6. Comparison of transmittance measurements from the microCT experiment and HADES simulation. Blue: microCT. Red: HADES. Object is half inch thick magnesium cylinder. Source is 100keV + Aluminum filter. Inset shows an enlarged view of transmittance values close to the thickest part of cylinder.

We have chosen to use effective linear attenuation coefficient (LAC) as the metric of comparison between microCT measurements and HADES simulations. The linear attenuation,  $\mu$ , of a material depends on the spectrum, the density of the material, and the chemical composition of the material. As the X-ray photons traverse the material and are absorbed, the spectrum changes. Typically, the lower energy X-rays are more strongly absorbed, and so the average energy of the spectrum increases and the rate of attenuation ( $\mu$ ) decreases with thickness. This is called "beam hardening."

While it is an approximation, we can provide an averaged linear attenuation coefficient for a particular thickness.

To obtain the LAC, we first identified the column of pixels corresponding to the thickest part of the cylinder by finding the local minimum of the average transmittance across the 10 selected rows of pixels. LAC is computed using the formula  $\mu = -\ln(I/I_0)/L$ , where  $L$  is pathlength of X-ray, or the diameter of the cylindrical object and  $I/I_0$  is transmittance. The average LAC at the thickest part through the material is taken as the effective LAC for the sample. Uncertainty in the measured  $\mu_{\text{microCT}}$  is estimated from the standard deviation of  $\mu$  at the thickest part of the object across the 10 rows. Similar procedure is used to obtain  $\mu_{\text{HADES}}$  from the HADES model. Tables 2A-D compare the effective linear attenuation coefficients values between microCT and HADES for all samples under each of the four X-ray energy spectra: 100keV + Aluminum filter, 160keV + Aluminum filter, 160keV + Aluminum and copper filters, and 300keV + copper filter.

Material	D	$\mu_{\text{microCT}}$	$\mu_{\text{HADES}}$	%diff	$2\sigma/\mu_{\text{microCT}}$
Graphite	0.5"	0.037	0.037	-0.1%	2.9%
	1"	0.033	0.033	0.0%	1.5%
	2"	0.035	0.034	-1.7%	1.0%
Delrin	0.5"	0.034	0.034	-1.2%	2.5%
	1"	0.033	0.033	-0.4%	1.3%
	2"	0.032	0.032	0.0%	0.7%
Water	0.5"	0.027	0.028	2.8%	1.8%
	1"	0.029	0.029	0.6%	1.1%
	2"	0.025	0.025	-0.9%	1.3%
Teflon	0.5"	0.055	0.054	-2.0%	1.4%
	1"	0.052	0.051	-1.4%	1.1%
	2"	0.048	0.048	-0.5%	1.6%
Aluminum	1"	0.098	0.093	-5.4%	0.8%
Alum Alloy	1"	0.098	0.097	-0.6%	0.8%
Magnesium	0.5"	0.070	0.069	-1.6%	1.1%
	1"	0.058	0.061	4.9%	0.7%
Silicon	0.5"	0.103	0.108	5.4%	1.3%
	1"	0.088	0.092	5.3%	1.2%
Titanium	0.5"	0.301	0.299	-0.5%	2.2%

Table 2A. Comparison of effective LAC computed from microCT data and HADES simulation using 100keV+Al filter X-ray spectrum. **D**: nominal diameter of the material. In HADES calculations, precise measurement of the sample thickness was used. **%diff** =  $(\mu_{\text{HADES}} - \mu_{\text{microCT}}) / \mu_{\text{microCT}}$ .  **$\sigma$** : standard deviation of microCT measurements.

Material	D	$\mu_{\text{microCT}}$	$\mu_{\text{HADES}}$	%diff	$2\sigma/\mu_{\text{microCT}}$
Graphite	0.5"	0.034	0.034	0.1%	2.1%
	1"	0.031	0.031	0.7%	1.9%
	2"	0.032	0.032	-1.0%	0.8%
Delrin	0.5"	0.030	0.030	-0.4%	4.1%
	1"	0.030	0.030	-0.4%	1.7%
	2"	0.029	0.029	0.0%	1.2%
Water	0.5"	0.024	0.025	2.9%	2.5%
	1"	0.026	0.026	0.8%	1.0%
	2"	0.022	0.022	-0.1%	0.7%
Teflon	0.5"	0.045	0.047	3.2%	2.1%
	1"	0.045	0.045	-0.3%	1.3%
	2"	0.043	0.043	0.5%	0.9%
Aluminum	1"	0.080	0.077	-3.9%	0.8%
Alum Alloy	1"	0.080	0.080	0.4%	0.8%
Magnesium	0.5"	0.056	0.055	-0.7%	1.4%
	1"	0.050	0.050	0.0%	1.3%
Silicon	0.5"	0.081	0.086	5.6%	0.8%
	1"	0.072	0.075	4.3%	0.7%
Titanium	0.5"	0.228	0.228	0.2%	1.0%

Table 2B. Comparison of effective LAC computed from microCT data and HADES simulation using 160keV+Al filter X-ray spectrum.

Material	D	$\mu_{\text{microCT}}$	$\mu_{\text{HADES}}$	%diff	$2\sigma/\mu_{\text{microCT}}$
Graphite	0.5"	0.028	0.028	1.4%	2.8%
	1"	0.025	0.026	2.4%	1.6%
	2"	0.027	0.027	1.4%	1.9%
Delrin	0.5"	0.024	0.024	0.6%	4.1%
	1"	0.024	0.024	0.5%	2.3%
	2"	0.023	0.024	1.2%	1.4%
Water	0.5"	0.018	0.019	4.7%	5.5%
	1"	0.020	0.020	1.5%	2.3%
Water	2"	0.017	0.018	1.3%	1.4%
Teflon	0.5"	0.033	0.034	2.1%	3.9%
	1"	0.033	0.034	1.3%	2.1%
	2"	0.033	0.034	3.1%	1.3%
Aluminum	1"	0.052	0.051	-1.7%	1.5%
	Alum Alloy	1"	0.052	0.053	1.5%
Magnesium	0.5"	0.032	0.033	2.0%	2.8%
	1"	0.032	0.032	1.2%	2.4%
Silicon	0.5"	0.046	0.049	7.2%	1.5%
	1"	0.046	0.048	5.1%	1.7%
Titanium	0.5"	0.134	0.141	5.6%	1.3%

Table 2C. Comparison of effective LAC computed from microCT data and HADES simulation using 160keV+Al and Cu filters X-ray spectrum.

Material	D	$\mu_{\text{microCT}}$	$\mu_{\text{HADES}}$	%diff	$2\sigma/\mu_{\text{microCT}}$
Graphite	0.5"	0.025	0.026	2.9%	2.7%
	1"	0.023	0.024	2.7%	1.9%
	2"	0.024	0.025	4.5%	1.7%
Delrin	0.5"	0.021	0.022	2.7%	5.7%
	1"	0.021	0.022	2.2%	2.5%
	2"	0.021	0.021	3.2%	1.5%
Water	0.5"	0.017	0.018	3.9%	6.7%
	1"	0.018	0.018	3.6%	2.4%
	2"	0.015	0.016	3.6%	1.2%
Teflon	0.5"	0.029	0.030	3.4%	3.0%
	1"	0.030	0.030	2.3%	1.9%
	2"	0.029	0.030	6.4%	1.5%
Aluminum	1"	0.042	0.042	1.9%	1.9%
	Alum Alloy	1"	0.042	0.043	3.9%
Magnesium	0.5"	0.027	0.027	3.0%	5.9%
	1"	0.026	0.027	3.8%	2.2%
Silicon	0.5"	0.037	0.039	7.7%	2.4%
	1"	0.037	0.039	6.8%	1.7%
Titanium	0.5"	0.090	0.097	8.0%	1.7%

Table 2D. Comparison of effective LAC computed from microCT data and HADES simulation using 300keV+Cu filter X-ray spectrum.

We carried out two HADES simulations for 1-inch aluminum sample, one using the composition of 100% aluminum, the second using the nominal elemental composition of 6061-T6 aluminum alloy, which contains magnesium and silicon as its major alloying elements. Results of these two simulations and their comparisons with the microCT measurement of the 1-inch aluminum cylinder are listed in Tables 2A-D under 'Aluminum' and 'Alum Alloy'. While the exact composition of the aluminum cylinder used in the microCT experiment is unknown, comparisons with HADES simulations show a clear improvement of the model's agreement with data at the three lower X-rays energies. The error reduced from -5.4% to -0.6% for the 100keV+Al filter X-ray, -3.9% to 0.4% for the 160keV+Al filter X-ray, and -1.7% to 1.5% for the 160keV+Al and Cu filter X-ray. The error increased from 1.9% to 3.9% at the highest energy 300keV + Cu filter X-ray, but this is below the 4.2% average error for

this X-ray source, as errors increased for all samples tested at 300keV (more discussion below). This improvement illustrates that HADES's ability to predict microCT experimental outcome depends critically on the accuracy with which we can specify the composition of a material. More accurate composition yields better modeling agreement with data. Because the exact composition of aluminum alloy is not clear, we have excluded aluminum from the discussion below and only considered the other 17 samples tested. All analyses below on modeling errors are carried out on absolute values.

## V. DISCUSSIONS

The magnitude of the discrepancy in LAC values between HADES and microCT ranges from 0.0% to 8.0%, with a mean absolute value of 2.4% and. This discrepancy tends to increase with higher X-ray energy. For example, for half-inch titanium, discrepancy in LAC was -0.5% under the source spectrum 100keV+ Al filter, and 8.0% under the source spectrum 300keV + Cu filter, the largest among all samples. The average absolute values of modeling errors was 1.7%, 1.2%, 2.5% and 4.2% for the X-ray spectra 100keV+Al, 160keV+Al, 160keV+Al+Cu and 300keV+Cu, respectively. One possible explanation for this trend is the way that HADES treats X-ray scattering. HADES includes losses due to scattering, but the code, being a simple ray-race, treats those losses identically as those due to absorption. Thus there is no pixel-to-pixel 'cross talk' in the simulated image. This approximation may have to be addressed in order to improve agreement between model and measurement at the higher energies, where Compton scatter tends to dominate the attenuation coefficient of the low-Z materials studied in this paper.

We used the standard deviation of microCT LAC measured across pixels spanning the center of the objects as an estimate of the measurement uncertainty. This uncertainty (normalized by the LAC) ranged from 0.7% to 6.7%. When taking this experimental measurement error into account, modeling error from HADES was often within the corresponding measurement uncertainty. For the 3 lower energy X-ray sources, modeling error was below measurement uncertainty in more than 70% of the samples, and for the 300keV X-ray source, modeling error was below measurement uncertainty in 23% of the cases (4 out of 17 samples).

The discrepancy also increases with effective atomic number of the material. Materials made of lighter elements – graphite, Delrin, water and Teflon – give smaller average errors: 1.0%, 0.9%, 1.8%, and 3.4% for the X-ray spectra 100keV+Al, 160keV+Al, 160keV+Al+Cu and 300keV+Cu, respectively. While materials made of heavier elements – magnesium silicon and titanium – give larger average errors: 3.5%, 2.2%, 4.2% and 5.8% for the four X-rays source settings, respectively. Since the magnitude of the photoelectric effect increases approximately as the fourth power of the atomic number, the trend of increasing discrepancy with atomic number may be an indication of an error in the spectral distribution of the source. Also, as atomic number increases,

the relative importance of Compton scattering increases, which is an effect not currently accounted for by HADES. In our future work, we plan to include the effect of Compton scattering in the sample material in our HADES model.

Other potential sources of error in the model are spectral accuracy and detector blur modeling. Our current detector blur modeling simulates spatial distribution of X-ray energy deposition in the scintillator layer as a function of incident X-ray energy, but it does not take into account backscattering from the glass nor direct response of photodiodes to X-ray and electrons. More experimental work needs to be carried out to evaluate these effects.

In conclusion, we have compared microCT experimental data and HADES simulations across 17 samples, 7 materials, and at 4 different X-ray spectra. On average, the predicted LAC differs from experimental outcome by 2.4%. The modeling error is within estimated measurement error in over 60% of the cases (42 out of 68 experiments). By analyzing the source of the discrepancy between model and experimental system, we are able to better understand the X-ray system, inform users of the X-ray system about its properties and suggest design improvements to enhance image quality. For example, if by including a model of scattering within the object in HADES we are able to greatly reduce or even remove the discrepancy between the model and data, then HADES has helped to point out the impact of scatter on the measurement. We believe, with more improvements and validation in the future, HADES can serve as a useful teaching tool for X-ray system development and evaluation.

## ACKNOWLEDGMENT

The authors would like to thank Dr. Jerel A. Smith for his comments and critiques on the manuscript.

## REFERENCES

- [1] M. B. Aufderheide, D. M. Slone, A. E. Schach von Wittenau, "HADES, A Radiographic Simulation Code," *Review of Progress in Quantitative Nondestructive Evaluation*, vol. 20A, AIP Conf. Proc. 557, pp. 507-513, 2000.
- [2] M. B. Aufderheide, G. Henderson, A. E. Schach von Wittenau, D. M. Slone, H. E. Martz, "HADES, a code for simulating a variety of radiographic techniques," 2004 IEEE Nuclear Science Symposium Conference Record, Volume 4, pp. 2579 – 2583, Digital Object Identifier 10.1109/NSSMIC.2004.1462780.
- [3] J. F. Briesmeister, "MCNP--A general Monte Carlo n-particle transport code", Technical Report LA-13709-M, Los Alamos National Laboratory, 2000.
- [4] D. E. Cullen et al., "Tables and Graphs of Photon-Interaction Cross Sections from 10 eV to 100 GeV Derived from the LLNL Evaluated Photon Data Library (EPDL), Parts A and B, UCRL-50400, Vol. 6A and 6B, Rev 4, 1989.
- [5] L. E. Butler and E. W. Edwards, "BRL-CAD Tutorial Series: Volume I – Overview and Installation", ARL-SR-113, February, 2002. Also see BRL-CAD website, brlcad.org.
- [6] J. H. Hubble, H. A. Gimm, and I. Overbo, "Pair, Triplet, and Total Atomic Cross Section's (and Mass Attenuation Coefficients) for 1 MeV-100 GeV Photons in Elements Z = 1 to 100", J. Phys. Chem. Ref. Data, Vol. 9, No.4, 1980, 1023-1147.
- [7] A. E. Schach von Wittenau, C. M. Logan, M. B. Aufderheide and D. M. Slone, Med. Phys. **29** (11), Nov. 2002, pp. 2559-2570.

This work performed under the auspices of the U.S. Department of Energy by Lawrence Livermore National Laboratory under Contract DE-AC52-07NA27344.